Applied Catalysis B: Environmental 233 (2018) 234–242

Contents lists available at ScienceDirect

Applied Catalysis B: Environmental

journal homepage: www.elsevier.com/locate/apcatb

Mechanistic modeling of solar photo-Fenton process with Fe^{3+}-EDDS at neutral pH

P. Soriano-Molina[a,b], J.L. García Sánchez[a,b], O.M. Alfano[c], L.O. Conte[c], S. Malato[d], J.A. Sánchez Pérez[a,b,*]

[a] Solar Energy Research Centre (CIESOL), Ctra de Sacramento s/n, ES04120, Almería, Spain
[b] Chemical Engineering Department, University of Almería, Ctra de Sacramento s/n, ES04120, Almería, Spain
[c] Instituto de Desarrollo Tecnológico para la industria Química (INTEC), Consejo Nacional de Investigaciones Científicas y Técnicas (CONICET) and Universidad Nacional del Litoral (UNL), Ruta Nacional N° 168, 3000, Santa Fe, Argentina
[d] Plataforma Solar de Almería, CIEMAT, Carretera Senés Km. 4, 04200, Tabernas, Spain

ARTICLE INFO

Keywords:
Acetamiprid
Kinetic model
Photon absorption
Raceway pond reactor
Solar radiation

ABSTRACT

This paper presents, for first time, a mechanistic model of the solar photo-Fenton process at neutral pH with the Fe^{3+}-EDDS complex for micropollutant removal, taking into account irradiance and reactor geometry. Due to its high photon absorptivity, this biodegradable complex allows high percentages of micropollutant removal to be achieved for short reaction times. Nonetheless, no model of the process with the Fe^{3+}-EDDS has yet been developed, meaning the proposed mechanism relies on photochemical reactions with the complex previously reported, and hypotheses deduced from experimental observation. The data for acetamiprid (ACTM) removal (100 μg L^{-1}) in stirred tank reactors with different liquid depths, under controlled conditions of irradiance and temperature, was used to obtain the model parameters. The model successfully fitted the experimental results obtained outdoors in a raceway pond reactor (RPR), with a change of scale from 0.85 to 19 L. For the calculation of the average volumetric rate of photon absorption (VRPA), the effect of the two components of solar UV radiation (direct and diffuse) as a function of the environmental conditions and the reactor layout was considered. The results showed an important contribution by diffuse radiation, even at noon under spring conditions (≈40% of the total VRPA). In addition, the applicability of the model has been demonstrated in water matrices containing organic matter and HCO_3^-/CO_3^{2-} ions, usually found in secondary wastewater treatment plant (WWTP) effluents. This approach allows for the development of control and optimization tools for the photo-Fenton process at neutral pH in low-cost photoreactors.

1. Introduction

Advanced Oxidation Processes (AOPs) have been proposed as a tertiary wastewater treatment for micropollutant removal [1,2]. These pollutants are organic compounds such as pesticides, pharmaceuticals and hormones which are not completely removed by WWTPs. Although micropollutants are discharged into natural water bodies at very low concentrations (ng L^{-1}-μg L^{-1}), they have a bioaccumulative character and toxic effect on organisms [3,4]. Among AOPs, the photo-Fenton process is one of the most efficient treatments [5]. It involves the oxidation of organic matter with the hydroxyl radicals generated by a redox cycle between hydrogen peroxide and ferrous iron under UV–vis radiation. This process is strongly dependent on parameters such as reactant concentration, irradiance, temperature, reactor layout and pH of water [6]. Although the optimum pH to run the process is 2.8, the treatment at neutral pH has been proposed to reduce operating costs, albeit with the disadvantage of iron precipitation [7]. As a remedy for this, polycarboxilic compounds, such as citrate, oxalate, maleate and ethylennediamine-*N*,N'-disuccinic acid (EDDS) are currently being investigated. They form a complex with iron, being maintained in solution and with fast photochemical reactions taking place under solar UV radiation [8–10]. Among these chelating agents, EDDS is a biodegradable structural isomer of EDTA, efficient in the pH range 3–9 [11]. In recent years, the number of publications on photo-Fenton with Fe^{3+}-EDDS has increased hugely, with degradation rates greater than 80% for short reaction times being reported [12–17]. In addition, a higher photon absorption of iron complexed with EDDS, compared to iron aquo complexes, has been reported [18].

Nowadays, the focus of many industries and researchers is to model and optimize wastewater treatment processes. To facilitate this, the

* Corresponding author at: Department of Chemical Engineering, University of Almería, 04120, Almería, Spain.
E-mail address: jsanchez@ual.es (J.A. Sánchez Pérez).

https://doi.org/10.1016/j.apcatb.2018.04.005
Received 2 February 2018; Received in revised form 24 March 2018; Accepted 2 April 2018
Available online 07 April 2018
0926-3373/

development of instrumentation, control and automation systems of WWTPs plays a fundamental role. It is essential to use computer tools based on mathematical models to optimize their design and development by means of simulation. Regarding the photo-Fenton process, several models to estimate the kinetics of micropollutant removal at acidic pH have been developed [19–22]. At pH close to neutrality, the modeling of the process has been widely studied using the ferrioxalate complex [23–26]. However, despite the large number of publications which highlight the interest of the scientific community in the use of Fe^{3+}-EDDS, a mechanistic model which includes photon absorption has not yet been proposed, to the best of the author's knowledge. Furthermore, most models have been developed in demineralized water matrices. Due to the effect of organic matter and HCO_3^-/CO_3^{2-} ions ($HO^{\bullet}$ scavengers) on the process, the inclusion of these species in the modeling could be of interest for a wider application.

The main goal of this work is to develop a mechanistic model of the solar photo-Fenton process with the Fe^{3+}-EDDS complex at neutral pH as a function of irradiance and reactor geometry for micropollutant removal. ACTM is frequently used as a model microcontaminant because it is a highly recalcitrant pesticide [27] included in a first watch list of priority hazardous substances [28]. To obtain the model parameters, experimental ACTM degradation data from a synthetic secondary effluent was used. These assays were conducted at lab scale under controlled conditions of irradiance (10–50 W m^{-2}) and temperature (25 °C). The kinetic model was validated outdoors in winter and spring conditions, with a change of scale from 0.85 L to 19 L in a RPR. These low-cost reactors have the advantage of being able to vary the liquid depth to achieve optimum use of photons, according to the availability of UV radiation and iron concentration. Moreover, they are more efficient regarding micropollutant removal (mass of micropollutant per surface of photoreactor) than the conventional tubular photoreactors with compound parabolic collectors (CPCs) [17]. The effect of photon absorption corresponding to diffuse UV light is included in the activated steps of the reaction mechanism. This component of solar radiation, not usually considered for photon absorption calculations, could account for a high percentage of total radiation in flat photoreactors, especially in winter or under cloudy conditions [29,30].

2. Experimental

2.1. Chemicals

Sodium hydroxide and sulphuric acid (98%) were purchased from J.T Baker®. Hydrogen peroxide (33%), ammonium nitrate, ferric sulphate (75%), hydrochloric acid (37%), acetic acid and $CaSO_4 \cdot H_2O$ were obtained from Panreac. Acetamiprid ($C_{10}H_{11}ClN_4$, 20% w/w) was purchased from EPIK®. Sodium formate was acquired from Merck Millipore and HPLC grade Acetonitrile from BDH Prolabo Chemicals. Peptone and beef extract were obtained from BD Bacto and Biolife, respectively. Ethylenediamine disuccinic acid (35%), titanium (IV) oxysulfate, ortho-phenantroline, peptone, sodium lauryle sulfonate, $MgSO_4$, acacia gum powder, sodium lignin sulfonate, ascorbic acid, arabic acid, formic acid (98%), $(NH_4)_2SO_4$, KCl, tetrabutylammonium bisulfate, methanol and humic salt were purchased from Sigma-Aldrich.

2.2. Experimental set-up

A synthetic secondary effluent with a Dissolved Organic Carbon (DOC) concentration of around 12 mg L^{-1} and 14 mg L^{-1}. Total Inorganic Carbon (IC) was used as a water matrix, according to [31,32]. Initial and final pH in the 7.0–7.5 range were recorded for each assay. In all the experiments, the ACTM, H_2O_2 and Fe^{3+} concentrations were 100 μgL^{-1} (representing the total concentration of micropollutant in secondary effluents) 0.88 mM (30 mg L^{-1}) and 0.1 mM, respectively. The Fe^{3+}-EDDS complex was prepared with 1:1 stoichiometry [11], as described in previous work [18].

The data obtained in cylindrical PVC stirred tank reactors, under controlled conditions to study the effect of VRPA on the kinetics of micropollutant removal, [18] was used to obtain the model parameters. The reactors (0.85 L volume, 15 cm diameter) were placed inside a SunTest CPS + solar box from Atlas, with an emission range from 250 to 765 W m^{-2}. The UVA irradiance range in the reactor surface was set from 10 to 50 W m^{-2} and the liquid depth was increased from 5 to 15 cm, keeping temperature constant at 25 °C with a cooling coil connected to a thermostatic bath. This temperature was set accordingly for experimentation because it is the average annual temperature recorded at the WWTP in Almeria, located in southeastern Spain. To avoid any incoming radiation through the reactor walls, they were made opaque (in PVC). Irradiance was measured on the reactor surface with a spectroradiometer (Avantes AvaSpec Dual-Cannel Fiber Optic Spectrometer), the wavelength range being 327 to 384 nm. This wavelength range was set because it is the wavelength range of the measurements given by the radiometer used in outdoor experiments.

For the model validation, experiments were conducted outdoors at the Solar Energy Research Centre (CIESOL) in Almería, Spain, in a 19-L PVC-RPR with 5 cm liquid depth and 22 cm channel width. The mixing time was low (2 min) compared to the reaction time (tens of minutes); hence the hypothesis of perfect mixing could be assumed. Temperature and pH were monitored online with probes connected to a LabJack USB/Ethernet data acquisition device. Incident UV radiation (direct and diffuse), averaged over the wavelength range 327–384 nm, was measured with a global UV radiometer (Delta Ohm, LPUVA02AV).

2.3. Chemical analysis

The samples collected from the reactor were filtered through 0.20-μm Millipore filters. After that, the filter was washed with acetonitrile (10:1, sample: acetonitrile), which stops the reaction and draws out any trace of contaminant retained [33].

Total dissolved iron was determined by the 1,10-phenanthroline method (ISO 6332), the limit of quantification (LOQ) being 4.5 10^{-3} mM. Hydrogen peroxide was quantified according to the spectrophotometric method DIN 38 402 H15, the LOQ being 2.9 10^{-2} mM.

Fe^{3+}-EDDS and ACTM concentrations were determined by liquid chromatography (HPLC Agilent 1100 Series and HPLC Agilent 1200 Series, respectively). For Fe^{3+}-EDDS, the mobile phases were methanol and an aqueous solution of sodium formiate (15 mM) and tetrabutylamonium hydrogen sulfate (2 mM) at pH 4. The LOQ was 1.8 10^{-3} mM. For ACTM, the phases were acetonitrile and dilute formic acid (0.1%, v/v). The LOQ was 5 μg L^{-1}. Methods and equipment characteristics were previously reported [18,22].

TIC and DOC concentrations were determined in a Shimadzu-V CPH TOC analyser, the LOQ being 2 mg L^{-1}.

2.4. Determination of the average volumetric rate of photon absorption (VRPA)

2.4.1. Experiments in a solar box

In a photoreactor, in which radiation emission is in parallel planes (the variation of the radiation can be considered as a function of a single spatial coordinate), and the scattering effect of the radiation can be considered negligible, the local volumetric rate of photon absorption (LVRPA) of an absorbent species can be determined by Eq. (1) [24,34]:

$$LVRPA\ (t, x) = q_{w,\lambda} \cdot k_\lambda(t) \cdot \exp(-k_{T,\lambda}(t) \cdot x) \quad (1)$$

where $q_{w,\lambda}$ is the spectral distribution of incident radiation (lamp power) at a specific wavelength (W m^{-2} nm^{-1}), k_λ is the volumetric absorption coefficient of the photon absorbing species (m^{-1}), $k_{T,\lambda}$ is the total volumetric absorption coefficient of the medium (m^{-1}) and x is the spatial coordinate (m). $q_{w,\lambda}$ was measured in the wavelength range

327–384 nm with a spectroradiometer (Avantes AvaSpec Dual-Cannel Fiber Optic Spectrometer), and Planck's equation was used to convert data from W m^{-2} to μE m^{-2} s^{-1}.

In perfect mixing systems, in which the concentration of species can be considered the same for any position in the reactor, the LVRPA can be averaged across the reactor volume [24,31,35–38]. Therefore, the average VRPA in the reactor for each of the absorbing species (Fe^{3+}-EDDS and Fe^{3+}-$EDDS_{ox}$, defined in 2.5) was calculated by integrating Eq. (1) over the liquid depth, D (m), Eqs. (2) and (3), since the reactor surface was constant. Due to the reactor layout inside the solar box, the light rays could be considered as being parallel in the direction perpendicular to the reactor surface. The change in Fe^{3+}-EDDS concentration over time was also taken into account.

$$VRPA_1(t) = \frac{1}{D}\sum_{\lambda}\frac{q_{w,\lambda}\cdot k_{Fe^{3+}-EDDS,\lambda}(t).\,[1-\exp(-k_{T,\lambda}(t)\bullet D)]}{k_{T,\lambda}(t)} \quad (2)$$

$$VRPA_2(t) = \frac{1}{D}\sum_{\lambda}\frac{q_{w,\lambda}\cdot k_{Fe^{3+}-EDDSox,\lambda}(t).\,[1-\exp(-k_{T,\lambda}(t)\bullet D)]}{k_{T,\lambda}(t)} \quad ((3))$$

The molar absorptivity of Fe^{3+}-EDDS (mM^{-1} m^{-1}), $\alpha_{Fe^{3+}-EDDS,\lambda}$ was determined from the UV absorption spectra obtained in synthetic secondary effluent, as previously reported [18]. As for Fe^{3+}-$EDDS_{ox}$, $\alpha_{Fe^{3+}-EDDSox,\lambda}$ was estimated from a photo-Fenton assay, assuming that once the experiment is started, the optical thickness of the solution at a given time is the sum of the optical thickness of all absorbent species, Eq. (4). Therefore, $\alpha_{Fe^{3+}-EDDSox,\lambda}$ could be isolated from Eq. (4). Finally, $k_{T,\lambda}$ could be calculated according to Eq. (5), [24].

$$\alpha_{\text{total dissolved Fe},\lambda}\cdot C_{\text{total dissolved Fe}} = \alpha_{Fe^{3+}-EDDS,\lambda}\cdot C_{Fe^{3+}-EDDS} + \alpha_{Fe^{3+}-EDDSox,\lambda}\cdot C_{Fe^{3+}-EDDSox} \quad (4)$$

where $\alpha_{\text{total dissolved Fe},\lambda}$ is the molar absorptivity of the medium, calculated from the UV absorption spectrum of dilutions of a sample taken after 5 min of the reaction, and measured instantaneously.

$$k_{T,\lambda}(t) = k_{Fe^{3+}-EDDS,\lambda} + k_{Fe^{3+}-EDDSox,\lambda} = \alpha_{Fe^{3+}-EDDS,\lambda}\cdot C_{Fe^{3+}-EDDS}(t) + \alpha_{Fe^{3+}-EDDSox,\lambda}\cdot C_{Fe^{3+}-EDDSox}(t) \quad ((5))$$

2.4.2. Outdoor experiments in an RPR

For experiments carried out in the RPR, the solar radiation that reaches the reactor surface is made up of direct radiation, which reaches the surface without being absorbed or scattered in the atmosphere, and diffuse radiation, that is, scattered radiation. Regarding direct radiation, its optical light path length depends on the solar zenith angle, θ_s, Fig. 1. The refracted angle inside the reactor, θ_{direct}, was estimated using Snell's law, assuming the refraction index of water matrix to be 1.33 [31]. Accordingly, for outdoor experiments, the expressions to calculate the average VRPA, Eqs. (2) and (3), were replaced by Eqs. (6) and (7):

Here, the value of $q_{wdirect,\lambda}$ is the product of the direct radiation and $\cos\theta_{direct}$.

$$VRPA_{direct1}(t) = \frac{1}{D}\sum_{\lambda}\frac{q_{wdirect,\lambda}\cdot k_{Fe^{3+}-EDDS,\lambda}(t)\cdot\left[1-\exp(-k_{T,\lambda}(t)\bullet\frac{D}{\cos\theta_{direct}})\right]}{k_{T,\lambda}(t)} \quad (6)$$

$$VRPA_{direct2}(t) = \frac{1}{D}\sum_{\lambda}\frac{q_{wdirect,\lambda}\cdot k_{Fe^{3+}-EDDSox,\lambda}(t)\cdot\left[1-\exp(-k_{T,\lambda}(t)\bullet\frac{D}{\cos\theta_{direct}})\right]}{k_{T,\lambda}(t)} \quad (7)$$

For the experiments in the solar box all the radiation could be considered direct and perpendicular to the reactor surface. However, due to the influence of the solar zenith angle on the UV radiation, the diffuse component was taken into account for outdoor experiments.

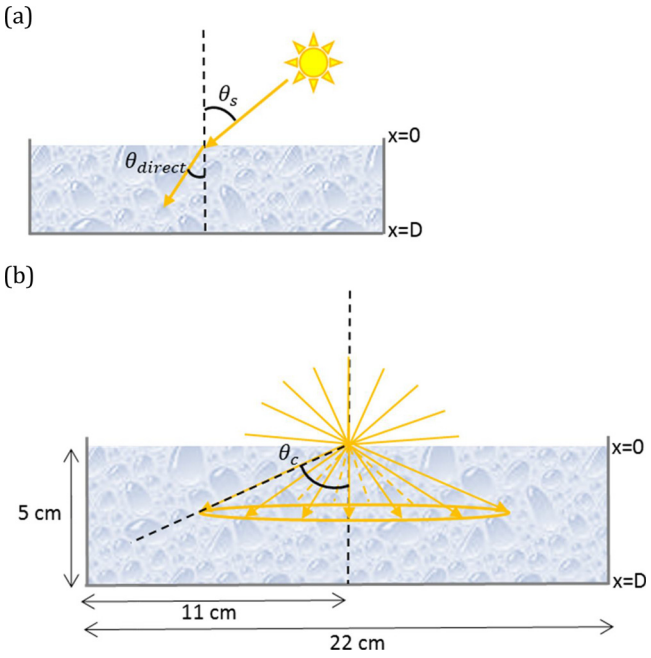

Fig. 1. Scheme for direct (a) and diffuse (b) light paths in a channel of the RPR (θ_c = 48.75°).

According to the Radiative Transfer Equation (RTE) [39], the LVRPA corresponding to the diffuse radiation can be determined by Eqs. (8) and (9), taking into account only photons moving towards the bottom of the reactor and azimuthal symmetry (propagation of rays as a function of the liquid depth, x, and an angular coordinate, $\theta_{diffuse}$),and the critical angle, θ_c, of the angular coordinate as a consequence of the refraction of light in the reactor [40].

$$LVRPA_{diffuse1}(x,\,t) = \sum_{\lambda} 2\cdot q_{wdiffuse,\lambda}\cdot k_{Fe^{3+}-EDDS,\lambda}(t)\cdot\int_0^{\theta_c} e^{-\frac{k_{T,\lambda}(t).x}{\cos\theta_{diffuse}}}\cdot \sin\theta_{diffuse}\,(d\theta_{diffuse}) \quad (8)$$

$$LVRPA_{diffuse2}(x,\,t) = \sum_{\lambda} 2\cdot q_{wdiffuse,\lambda}\cdot k_{Fe^{3+}-EDDSox,\lambda}(t)\cdot\int_0^{\theta_c} e^{-\frac{k_{T,\lambda}(t).x}{\cos\theta_{diffuse}}}\cdot \sin\theta_{diffuse}\,(d\theta_{diffuse}) \quad (9)$$

Finally, the reactor volume average LVRPA can be calculated by Eqs. (10) and (11):

$$VRPA_{diffuse1}(t) = \frac{1}{D}\cdot\int_0^D \sum_{\lambda} 2\cdot q_{w,\lambda}\cdot k_{Fe^{3+}-EDDS,\lambda}(t)\cdot\left(\int_0^{\theta_c} e^{-\frac{k_{T,\lambda}(t).x}{\cos\theta_{diffuse}}}\cdot\sin\theta_{diffuse}\,(d\theta_{diffuse})dx\right) \quad (10)$$

$$VRPA_{diffuse2}(t) = \frac{1}{D}\cdot\int_0^D \sum_{\lambda} 2\cdot q_{w,\lambda}\cdot k_{Fe^{3+}-EDDSox,\lambda}(t)\cdot\left(\int_0^{\theta_c} e^{-\frac{k_{T,\lambda}(t).x}{\cos\theta_{diffuse}}}\cdot\sin\theta_{diffuse}\,(d\theta_{diffuse})dx\right) \quad (11)$$

$q_{wdirect,\lambda}$ and $q_{wdiffuse,\lambda}$ were obtained with the solar software SMARTS2. This simple model estimates the atmospheric radiative transfer of sunshine from spectral transmittance functions for the main extinction processes in the atmosphere, such as Rayleigh scattering, ozone and aerosol extinction [41]. The SMARTS2 code prediction of the spectral distribution of UV radiation was determined at the latitude for the city of Almería, Spain (36°50´17´´N, 2°27´35´´W, at sea level). The main atmospheric conditions were characterized by the following input variables: the Angstrom's Beta and Schuepp's B coefficients for atmospheric turbidity (0.087 and 0.088, respectively), and the wavelength

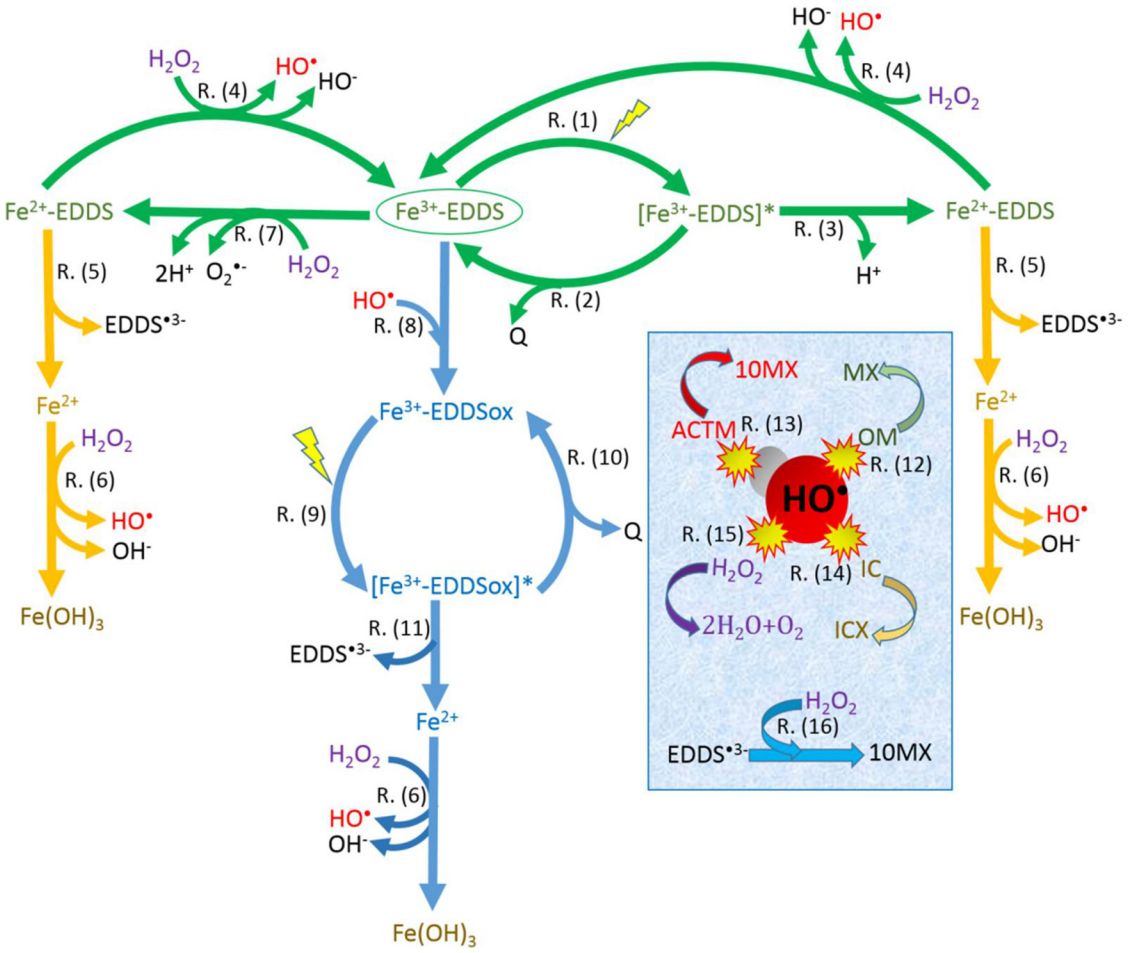

Fig. 2. Model reactions. Green, orange and blue arrows correspond to Fe^{3+}-EDDS, Fe^{2+}-EDDS and Fe^{3+}-$EDDS_{ox}$ paths, respectively (For interpretation of the references to colour in this figure legend, the reader is referred to the web version of this article).

exponents α_1 and α_2 (close to 0.9 and 1.2, respectively), obtained from the Shettle and Fenn urban aerosol model as a function of wavelength and humidity. The average values of direct and diffuse irradiance obtained from this model were corroborated by the measurement given by the global UV radiometer (Delta Ohm, LPUVA02AV).

2.5. Kinetic model

The iron precipitation and the presence of species, such as HCO_3^-/CO_3^{2-}ions, increase the complexity of the reaction system and, consequently, the process modeling at the natural pH of water. In line with previous work focused on the photochemical study of the Fe^{3+}-EDDS complex [11–13,18], a kinetic model has been proposed. It justifies the presence of iron in solution after complex decomposition, in addition to modeling the kinetics of the micropollutant degradation. The scheme for the reaction mechanism and rate equations are shown in Fig. 2 and Table 1, respectively. Once Fe^{3+}-EDDS is photoactivated by UV radiation, R. (1), a fraction of the absorbed radiation is used in iron reduction, R. (2), while another fraction is converted into heat (Q), with the complex returning to its initial state as Fe^{3+}-EDDS, R. (3), [18,22]. The formation of the Fe^{2+}-EDDS complex has been reported for the Fenton process, as well as for the activated persulfate process [42,43], and some authors have pointed out that once the complex is reduced, it is decomposed to Fe^{2+} and $EDDS^{\bullet 3-}$ [12,14]. Along the same lines, this study proposes that the photoreduced iron could remain as Fe^{2+}-EDDS, as an intermediate state, before being decomposed to Fe^{2+} and $EDDS^{\bullet 3-}$, R. (5). Consequently, Fe^{2+}-EDDS could be oxidized by H_2O_2 (Fenton) returning to its initial state as Fe^{3+}-EDDS [42,44]. It is known that Fe^{2+}-polycarboxylate complexes, such as ferrous-oxalate, react much faster with H_2O_2 than Fe^{2+} aquo complexes [23,45]. Therefore, the presence of Fe^{2+}-EDDS after the irradiation of Fe^{3+}-EDDS could explain the high H_2O_2 consumption for the first few minutes of reaction. Fe^{2+} reacts with H_2O_2 (classic Fenton, R. (6)) giving rise to $HO^{\bullet}$ and Fe^{3+}, which precipitates as $Fe(OH)_3$ at neutral pH instantaneously. Fe^{3+}-EDDS is also reduced by H_2O_2, R. (7) [42], through a much slower reaction than R. (2).

Table 1
Rate law equations.

Rate equation	Reaction number
$r_1 = VRPA_1$	R. (1)
$r_2 = k_2\,[[Fe^{3+}{-}EDDS]^{-*}]$	R. (2)
$r_3 = k_3\,[[Fe^{3+}{-}EDDS]^{-*}]$	R. (3)
$r_4 = k_4\,[Fe^{2+}{-}EDDS]\,[H_2O_2]$	R. (4)
$r_5 = k_5\,[Fe^{2+}{-}EDDS]$	R. (5)
$r_6 = k_6\,[Fe^{2+}]\,[H_2O_2]$	R. (6)
$r_7 = k_7\,[[Fe^{3+}{-}EDDS]^{-}]\,[H_2O_2]$	R. (7)
$r_8 = k_8\,[[Fe^{3+}{-}EDDS]^{-}]\,[HO^{\bullet}]$	R. (8)
$r_9 = VRPA_2$	R. (9)
$r_{10} = k_{10}\,[[Fe^{3+}{-}EDDS_{ox}]^{*}]$	R. (10)
$r_{11} = k_{11}\,[[Fe^{3+}{-}EDDS_{ox}]^{*}]$	R. (11)
$r_{12} = k_{12}\,[MO]\,[HO^{\bullet}]$	R. (12)
$r_{13} = k_{13}\,[ACTM]\,[HO^{\bullet}]$	R. (13)
$r_{14} = k_{14}\,[IC]\,[HO^{\bullet}]$	R. (14)
$r_{15} = k_{15}\,[H_2O_2]\,[HO^{\bullet}]$	R. (15)
$r_{16} = k_{16}\,[H_2O_2]\,[EDDS^{\bullet 3-}]$	R. (16)

Since these paths are not cyclic, iron would rapidly precipitate after being oxidized by H_2O_2. Nonetheless, experimental data showed a longer lifespan of iron in solution after complex decomposition, which could be explained by the presence of oxidized species of the complex (Fe^{3+}-$EDDS_{ox}$) derived from the oxidation of Fe^{3+}-EDDS with HO• radicals, R. (8) [18,42]. Moreover, the absorption of the oxidized complex was checked experimentally and calculated as described in Section 2.4.1. Thus, Fe^{3+}-$EDDS_{ox}$ could absorb radiation giving rise to Fe^{2+} and $EDDS^{\bullet 3-}$. The generated hydroxyl radicals also react with the organic matter (OM), R. (12), the model pollutant ACTM, R. (13), the inorganic carbon (IC), R. (14), and the H_2O_2, R.(15), giving rise to their respective oxidation products. Finally, $EDDS^{\bullet 3-}$ radicals are able to react with H_2O_2 giving rise to oxidized matter, R. (16).

3. Results and discussion

3.1. Model parameters estimation

Assuming the hypothesis of perfect mixing and operation in batch mode, the dynamic model was obtained by imposing mass balances on each of species of the system, Table 2. Since the mass balance to the oxidized organic matter was expressed in carbon moles, the reactions corresponding to the oxidation of the ACTM and $EDDS^{\bullet 3-}$, R. (13) and R. (16), were multiplied by 10 (the number of carbon atoms in both ACTM and EDDS) in Eq. (24). The set of differential equations was solved using the MATLAB function ode23s, and the model parameters were obtained by the built-in optimization routine: fmincon. The objective function was defined by Eq. (12), where the errors of each species are normalized and a weight is assigned to them, w_A, w_H, w_F and w_C. In order to achieve a good fit to reagent consumption and micropollutant removal, the highest weight was imposed for H_2O_2 consumption and ACTM degradation errors, while the lowest weight was assigned to that of the total dissolved iron: $w_A = 1$, $w_H = 1$, $W_F = 0.25$ and $w_C = 0.75$.

$$J = \sum_{j=1}^{m}\left[\sum_{i=1}^{n} w_A\cdot\left(\frac{A_{x(i,j)}-A_{m(i,j)}}{A_{x(1,j)}}\right)^2 + w_H\cdot\left(\frac{H_{x(i,j)}-H_{m(i,j)}}{H_{x(1,j)}}\right)^2 + w_F\cdot\left(\frac{F_{x(i,j)}-F_{m(i,j)}}{F_{x(1,j)}}\right)^2 + w_C\cdot\left(\frac{C_{x(i,j)}-C_{m(i,j)}}{C_{x(1,j)}}\right)^2\right] \quad (12)$$

Table 2
Dynamic model equations.

Mass balance model	Equation number
$\frac{d[[Fe^{3+}-EDDS]^-]}{dt} = -r_1 + r_2 + r_4 - r_7 - r_8$	Eq. (14)
$\frac{d\left[[Fe^{3+}-EDDS]^{-*}\right]}{dt} = r_1 - r_2 - r_3$	Eq. (15)
$\frac{d[Fe^{2+}]}{dt} = r_5 - r_6 + r_{11}$	Eq. (16)
$\frac{d[Fe^{2+}-EDDS]}{dt} = r_3 - r_4 - r_5 + r_7$	Eq. (17)
$\frac{d[Fe^{3+}-EDDSox]}{dt} = r_8 - r_9 + r_{10}$	Eq. (18)
$\frac{d[[Fe^{3+}-EDDSox]^*]}{dt} = r_9 - r_{10} - r_{11}$	Eq. (19)
$\frac{d[H_2O_2]}{dt} = -r_4 - r_6 - r_7 - r_{15} - r_{16}$	Eq. (20)
$\frac{d[HO^\bullet]}{dt} = r_4 + r_6 - r_8 - r_{12} - r_{13} - r_{14} - r_{15}$	Eq. (21)
$\frac{d[ACTM]}{dt} = -r_{13}$	Eq. (22)
$\frac{d[OM]}{dt} = -r_{12}$	Eq. (23)
$\frac{d[MX]}{dt} = r_{12} + 10\,r_{13} + 10\,r_{16}$	Eq. (24)
$\frac{d[IC]}{dt} = -r_{14}$	Eq. (25)
$\frac{d[ICX]}{dt} = r_{14}$	Eq. (26)
$\frac{d[EDDS^{\bullet 3-}]}{dt} = r_5 + r_{11} - r_{16}$	Eq. (27)

In Eq. (12), n is the number of data points in each experiment (n = 9), m is the number of assays used in the search for parameters from the total of 14 experimental conditions (m = 7) and finally, A, H, F and C are ACTM, H_2O_2, total dissolved iron and Fe^{3+}-EDDS concentration, respectively. Subscript x refers to experimental data and m to model data.

The root mean square error (RMSE) equation was used to calculate the error percentage between experimental data and model estimations for each species:

$$RMSE = \sqrt{\frac{1}{m\cdot n}\cdot\sum_{j=1}^{m}\sum_{i=1}^{n}\left(\frac{C_{i,x(i,j)}-C_{i,m(i,j)}}{C_{i,x(1,j)}}\right)^2}\cdot 100 \quad (13)$$

where $C_{i,x}$ and $C_{i,m}$ are the experimental and model estimated concentrations of total dissolved iron, H_2O_2, Fe^{3+}-EDDS and ACTM, respectively.

From the total of 14 kinetic constants, 3 were taken from literature: $k_6 = 4.56\ mM^{-1}\ min^{-1}$ (classic Fenton), $k_{14} = 5.1{\cdot}10^5\ mM^{-1}\ min^{-1}$ (HCO_3- oxidation by HO•) [46], and $k_{15} = 1.6{\cdot}10^6\ mM^{-1}\ min^{-1}$ (H_2O_2 oxidation by HO•) [47]. The estimated kinetic constants are shown in Table 3. Standard deviation for each constant was estimated by resampling the residuals of the best fit and implementing a bootstrap estimate to be used with the search algorithm of fmincon. The obtained standard deviations were assumable taking into account that the procedure was repeated for 500 times to get an estimation of the parameter distribution, statistical analysis being conducted over these distributions.

According to the determined parameters, most of the energy absorbed by the Fe^{3+}-EDDS is employed in its reduction, $k_3 > > k_2$, while that absorbed by its oxidized form, Fe^{3+}-$EDDS_{ox}$, is released into the medium as heat, $k_{10} > k_{11}$. This would appear to be logical, since the quantum efficiency of the Fe^{3+}-EDDS may well decrease after being oxidized. Concerning Fe^{2+}-EDDS oxidation by H_2O_2, R. (4), k_4 is three orders of magnitude higher than k_6 (classic Fenton). Although as far as the authors know the kinetic constant for Fe^{2+}-EDDS oxidation has not been reported, values as high as $1.86{\cdot}10^3 mM^{-1}min^{-1}$ (coincident with that determined for Fe^{2+}-EDDS in this work, $k_4 = 1.9{\cdot}10^3 mM^{-1}min^{-1}$) have been published for Fe^{2+}-oxalate oxidation [23] and mentioned in previous work with Fe^{3+}-EDDS [12]. Such a fast reaction rate between H_2O_2 and Fe^{2+}-EDDS points out the relevance of Fe^{2+}-EDDS being proposed as an intermediate state for the photo-Fenton process in this work. R. (7) is much lower than R. (3), in concordance with the slower Fenton reduction when compared to photo-Fenton [42] and the observation in previous Fenton assays, in which the concentration of the species hardly changed [18]. The resulting kinetic constant corresponding to the Fe^{3+}-EDDS oxidation by HO• radicals, k_8, is of the order of magnitude of that corresponding to Fe^{3+}-EDTA oxidation, $3.1{\cdot}10^7\ mM^{-1}min^{-1}$, a value which has been directly imposed on k_8 in certain studies [42]. Regarding the oxidation of organic compounds with the generated HO•, k_{13} is higher than k_{12}, which is consistent with the observation that the parent compound degrades much faster than the organic matter mineralizes [22].

Table 3
Model parameters obtained from minimizing the objective function.

Kinetic constant	Value	Standard deviation	Unit
k_2	0.25	0.095	min^{-1}
k_3	17.14	4.81	min^{-1}
k_4	$1.9{\cdot}10^3$	$0.23{\cdot}10^3$	$mM^{-1}\,min^{-1}$
k_5	35.69	4.09	min^{-1}
k_7	0.40	0.18	$mM^{-1}\,min^{-1}$
k_8	$5.6{\cdot}10^7$	$0.53{\cdot}10^7$	$mM^{-1}\,min^{-1}$
k_{10}	10.50	1.92	min^{-1}
k_{11}	3.31	0.55	min^{-1}
k_{12}	$6.2{\cdot}10^6$	$0.81{\cdot}10^6$	$mM^{-1}\,min^{-1}$
k_{13}	$6.4{\cdot}10^7$	$0.43{\cdot}10^7$	$mM^{-1}\,min^{-1}$
k_{16}	$1.2{\cdot}10^6$	$0.24{\cdot}10^6$	$mM^{-1}\,min^{-1}$

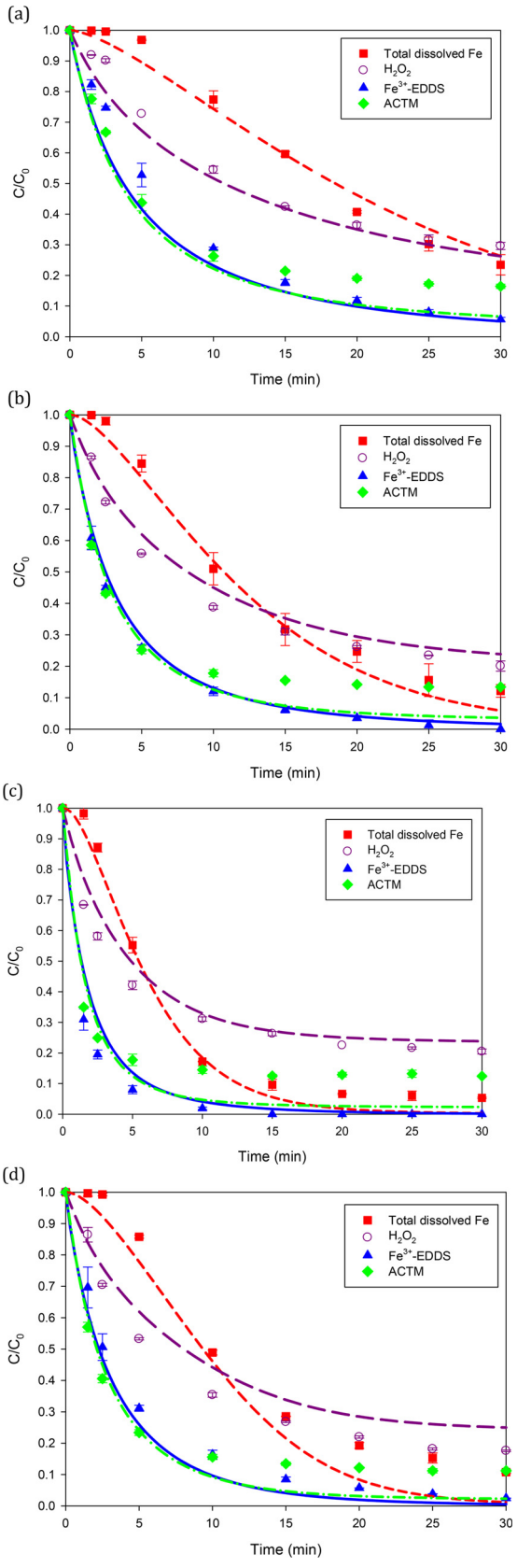

Fig. 3. Total dissolved iron, H_2O_2, Fe^{3+}-EDDS and ACTM profiles as a function of irradiance and liquid depth: 10 W m^{-2} and 5 cm (a), 20 W m^{-2} and 5 cm (b) 50 W m^{-2} and 5 cm (c), 40 W m^{-2} and 15 cm (d). Lines represent model estimations (short dashes for total dissolved iron, long dashes for H_2O_2, solid for Fe^{3+}-EDDS, and dash-dot for ACTM).

Despite the complexity of the reaction medium (a synthetic secondary WWTP effluent at neutral pH), the proposed model acceptably fits the experimental data for all the experimental conditions, both at 5 and 15 cm liquid depth. The RMSE was 5.6%, 6.8%, 5.4% and 7.2% for total dissolved iron, H_2O_2, Fe^{3+}-EDDS and ACTM, respectively. Fig. 3 shows the comparison between kinetic data predicted by the model and experimental results obtained in the solar box for 4 selected conditions, corresponding to the different seasons of the year. As can be seen, the model adequately reproduces the presence of iron in solution after complex decomposition, with an acceptable fit. As for H_2O_2 consumption, the simulation results show a good fit to the experimental data over 30 min of reaction. Due to the process is photosaturated at 40 W m^{-2} and 5 cm [18], Fig. 3(d) shows the model predictions when the liquid depth is increased. In this case, the model also fits the data, with a slightly slower reaction rate predicted for H_2O_2, pointing out that the model could be useful for predicting the treatment capacity by optimizing the liquid depth to take advantage of the photons that reach the reactor surface, at these mild oxidation conditions. In all the cases, the model reproduces almost exactly experimental data for ACTM removal in the first 5 min of the reaction and with good prediction until 10 min. After that, according to the experimental results, the ACTM degradation is stopped and the model predicts a slight drop in its concentration, the error in micropollutant removal being around 10% at 30 min. This deviation could be due to that once the complex concentration is low (due to its degradation), the generation rate of HO• radicals is lower and ACTM removal is stopped due to competence with organic matter (in the range of tens of mg L^{-1}) that could easier react with HO• radicals and other radicals formed during the process. Legislation in Switzerland demands 80% micropollutant removal in WWTPs, from the entrance to the exit of the WWTP [48]. Taking into account that this error between the experimental and simulated data occurs when ≥ 80% micropollutant removal has been directly achieved in the photo-Fenton process (tertiary treatment), this overestimation would not be very significant when using the model in practical applications.

3.2. Outdoor model performance

The kinetics parameters, obtained from experiments in the solar box under controlled conditions of irradiance and temperature, were used to validate the model with experimental data obtained outdoors in an RPR with 5 cm liquid depth. The assays were conducted at noon during winter and spring days and the temperature was in the range 20–30 °C. Within this range, the change in molar absorptivity can be considered negligible [22], thus it was assumed to be the same as that calculated for indoor experiments. Due to the fact that the direct beams only reach the illuminated zones of the reactor, whereas diffuse beams reach all the zones, the reactions R. (1) and R. (9) were modified accordingly:

$$r_1 = \frac{V_i}{V}VRPA_{direct1} + VRPA_{diffuse1} \qquad \text{R. ((17))}$$

$$r_9 = \frac{V_i}{V}VRPA_{direct2} + VRPA_{diffuse2} \qquad \text{R. ((18))}$$

where V_i and V denote irradiated and reaction volume, respectively. Vi was calculated taking into account the dark areas generated by the reactor walls as a function of the solar zenith angle. In all the experiments V was 19 L.

As can be observed in Fig. 4, outdoor experimental data reproduces the phenomenon observed in the experiments carried out in the solar simulator. As a result, both for winter and spring conditions, values close to 70% and 80% of H_2O_2 consumption and ACTM degradation, respectively, were achieved. The model resulted in a successful fit to the experimental data of H_2O_2 consumption, total dissolved iron profile, Fe^{3+}-EDDS decomposition and ACTM degradation for winter conditions. The RMSE values were 1.1%, 5.9%, 1.9% and 4.3%, respectively. As for spring conditions, Fig. 4(b), the model reproduces H_2O_2 consumption and the

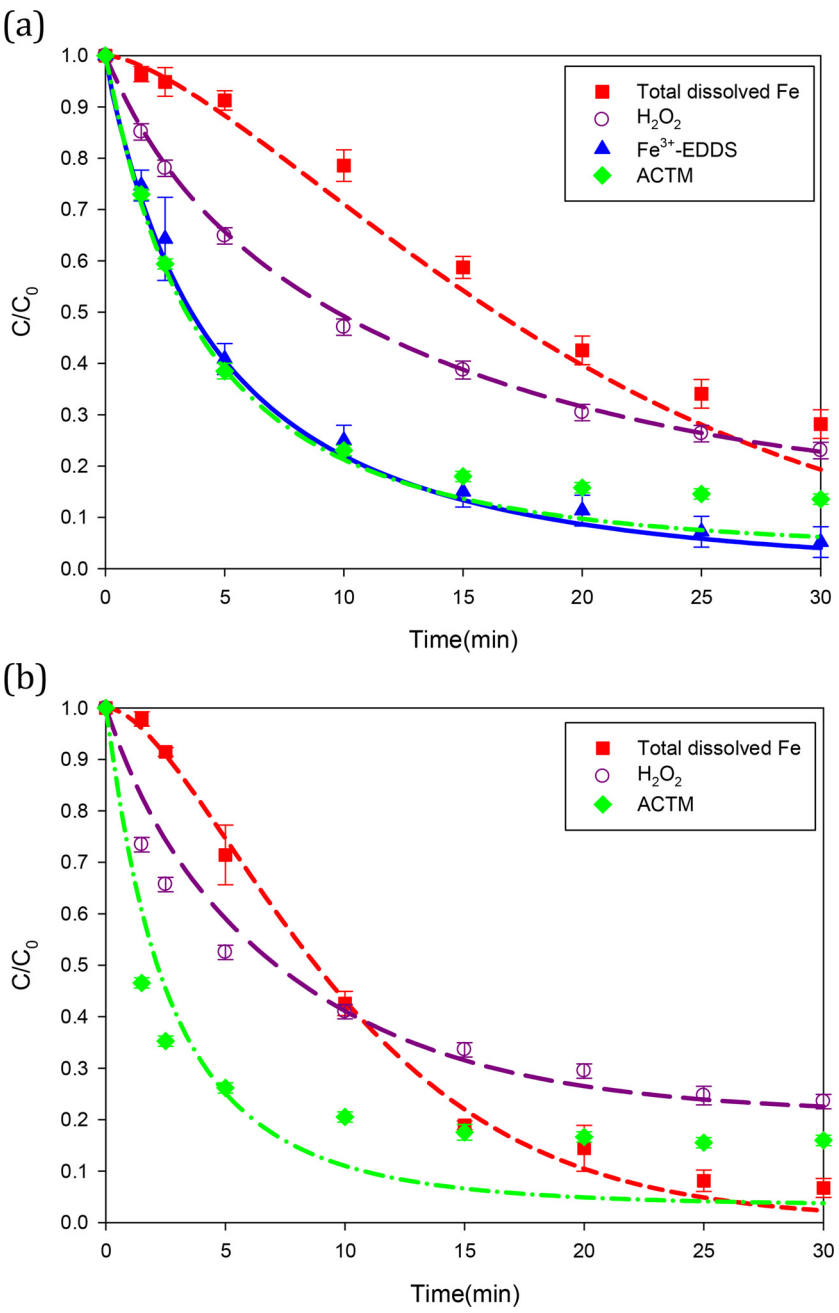

Fig. 4. Model validation in an RPR with 5 cm liquid depth in winter (a) and spring (b) conditions (Winter: average water temperature: 21.1 °C, θ_s = 58.24°, direct irradiance = 5.86 W m^{-2}, diffuse irradiance = 10.09 W m^{-2}, V_i = 16.1 L. Spring: average water temperature: 28.3 °C, θ_s = 27.13°, direct irradiance = 18.69 W m^{-2}, diffuse irradiance = 13.38 W m^{-2}, V_i = 17.3 L). Lines represent model estimations (short dashes for total dissolved iron, long dashes for H_2O_2, solid for Fe^{3+}-EDDS, and dash-dot for ACTM).

total dissolved iron profile, with a RMSE value of 5.0% and 2.8%, respectively. The experimental data of ACTM is reproduced for the first 5 min of the reaction. Subsequently, after 80% ACTM degradation, an overestimation in its removal rate is observed, as in the experiment at lab scale, the total RMSE being 9.9%. These results show that the kinetics model, obtained from lab scale data in cylindrical stirred reactors, could be applied on a larger scale to perfectly mixed reactors of different geometry, such as RPRs. The model could therefore be useful for optimizing the treatment capacity in WWTPs as a function of the availability of UV radiation.

It is worth mentioning the contribution of diffuse irradiance towards the kinetics of the process, whose value represents more than 50% of the total irradiance at noon in winter (63% in the experimental condition shown in Fig. 4(a)). Fig. 5 shows the time-courses of VRPA values predicted by the model for Fe^{3+}-EDDS and Fe^{3+}-$EDDS_{ox}$ for the best radiation condition (spring). At the beginning of the reaction, the VRPA values corresponding to direct and diffuse radiation for Fe^{3+}-EDDS were 643 μE m^{-3} s^{-1} and 462 μE m^{-3} s^{-1}, respectively, pointing out the effect of diffuse radiation on the kinetics of the process, even under clear day conditions in spring. Furthermore, as mentioned above, the decrease in the Fe^{3+}-EDDS concentration, observed in all experimental conditions, has an important effect on photon absorption. In this case, the VRPA is reduced by more than three times after 5 min of the reaction. Nonetheless, the VRPA due to the Fe^{3+}-EDDSox complex increases in the first few minutes, being equal to the VRPA due to the parent complex (Fe^{3+}-EDDS) at 3.5 min of reaction. Despite this increase in the VRPA of the oxidized species, most of the radiation absorbed by them is released as heat, as mentioned above. These results agree with the low reaction rates observed after 5 min of the reaction, highlighting the relevance of the VRPA corresponding to the Fe^{3+}-EDDS, R. (1), on the kinetics of the process.

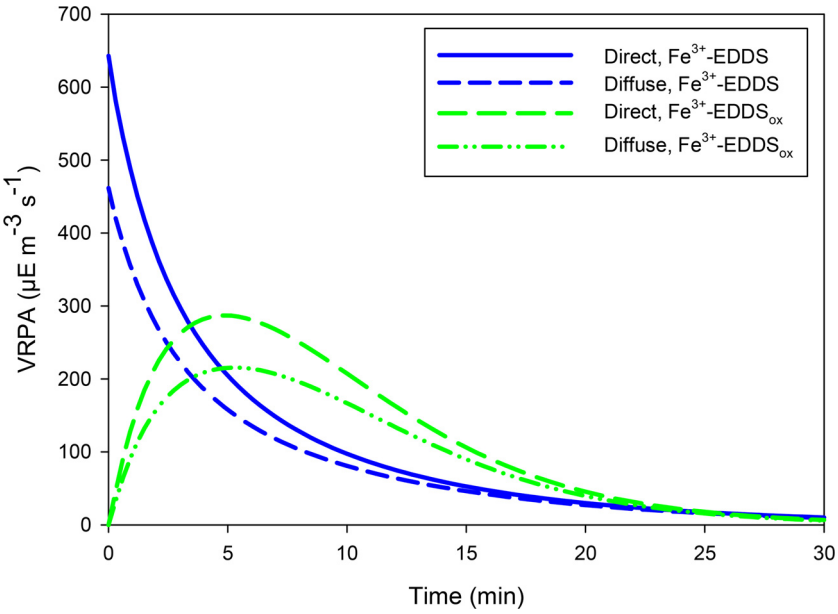

Fig. 5. Effect of decomposition and oxidation of Fe^{3+}-EDDS on direct and diffuse VRPA at noon in spring.

4. Conclusions

A mechanistic model of the photo-Fenton process in an effluent from a WWTP at neutral pH with the Fe^{3+}-EDDS complex is proposed for the first time. This model was developed based on previous kinetic studies and hypotheses deduced from experimental data. It was able to reproduce the kinetics of Fe^{3+}-EDDS decomposition, iron precipitation, H_2O_2 consumption and microcontaminant removal at short reaction times in complex water matrices. The importance of diffuse radiation on the kinetics of the process carried out in flat photoreactors was demonstrated, the diffuse VRPA representing values as high as 40% of the total VRPA at noon in spring. The model was successfully validated outdoors in an RPR, thus being, of great application for the control and optimization of the process in scalable and low-cost photocatalytic reactors.

Acknowledgements

This research was supported by the European Regional Development Fund (ERDF) and the Ministry for Economy and Competitiveness (Spanish Government), project CTM2015-71054-REDT and CTQ2016-78255-R. O.M. Alfano and L.O. Conte would like to acknowledge Universidad Nacional del Litoral (UNL), Consejo Nacional de Investigaciones Científicas y Técnicas (CONICET), and Agencia Nacional de Promoción Científica y Tecnológica (ANPCyT) for their financial support. P. Soriano-Molina is grateful to the Ministry of Education, Culture and Sport for her FPU scholarship (AP2014/01030) and the funding for her placement at Instituto de Desarrollo Tecnológico para la Industria Química (INTEC), Santa Fe (Argentina) (EST16/00602). Finally, the authors sincerely acknowledge G. Mailhot and M. Brigante, from Institut de Chimie de Clermont-Ferrand (France), for their verbal collaboration in the kinetic model formulation.

References

[1] N. Serpone, Y.M. Artemev, V.K. Ryabchuk, A.V. Emeline, S. Horikoshi, Light-driven advanced oxidation processes in the disposal of emerging pharmaceutical contaminants in aqueous media: a brief review, Curr. Opin. Green Sustain. Chem. 6 (2017) 18–33, http://dx.doi.org/10.1016/j.cogsc.2017.05.003.

[2] O.M. Rodriguez-Narvaez, J.M. Peralta-Hernandez, A. Goonetilleke, E.R. Bandala, Treatment technologies for emerging contaminants in water: A review, Chem. Eng. J. 323 (2017) 361–380, http://dx.doi.org/10.1016/j.cej.2017.04.106.

[3] R. Münze, C. Hannemann, P. Orlinskiy, R. Gunold, A. Paschke, K. Foit, J. Becker, O. Kaske, E. Paulsson, M. Peterson, H. Jernstedt, J. Kreuger, G. Schüürmann, M. Liess, Pesticides from wastewater treatment plant effluents affect invertebrate communities, Sci. Total Environ. 599–600 (2017) 387–399, http://dx.doi.org/10.1016/j.scitotenv.2017.03.008.

[4] D. Destrieux, F. Laurent, H. Budzinski, J. Pedelucq, P. Vervier, M. Gerino, Drug residues in urban water: A database for ecotoxicological risk management, Sci. Total Environ. 609 (2017) 927–941, http://dx.doi.org/10.1016/j.scitotenv.2017.07.043.

[5] I. Velo-Gala, J.A. Pirán-Montaño, J. Rivera-Utrilla, M. Sánchez-Polo, A.J. Mota, Advanced Oxidation Processes based on the use of UVC and simulated solar radiation to remove the antibiotic tinidazole from water, Chem. Eng. J. 323 (2017) 605–617, http://dx.doi.org/10.1016/j.cej.2017.04.102.

[6] A. Delavaran Shiraz, A. Takdastan, S. Mehdi Borghei, Photo-Fenton like degradation of catechol using persulfate activated by UV and ferrous ions: Influencing operational parameters and feasibility studies, J. Mol. Liq. 249 (2018) 463–469, http://dx.doi.org/10.1016/j.molliq.2017.11.045.

[7] L. Clarizia, D. Russo, I. Di Somma, R. Marotta, R. Andreozzi, Homogeneous photo-Fenton processes at near neutral pH: A review, Appl. Catal. B: Environ. 209 (2017) 358–371, http://dx.doi.org/10.1016/j.apcatb.2017.03.011.

[8] A.A. Nogueira, B.M. Souza, M.W.C. Dezotti, R.A.R. Boaventura, V.J.P. Vilar, Ferrioxalate complexes as strategy to drive a photo-FENTON reaction at mild pH conditions: A case study on levofloxacin oxidation, J. Photochem. Photobiol. A: Chem. 345 (2017) 109–123, http://dx.doi.org/10.1016/j.jphotochem.2017.05.020.

[9] J.A. Lima, A.L. Tonetti, C. Vidal, C.C. Montagner, R.F. Pupo Nogueira, Simultaneous degradation of ciprofloxacin, amoxicillin, sulfathiazole and sulfamethazine, and disinfection of hospital effluent after biological treatment via photo-Fenton process under ultraviolet germicidal irradiation, Appl. Catal. B: Environ. 224 (2018) 761–771, http://dx.doi.org/10.1016/j.apcatb.2017.11.021.

[10] D. Seibert, T. Diel, J.B. Welter, A.L. de Souza, A.N. Módenes, F.R. Espinoza-Quiñones, F.H. Borba, Performance of photo-Fenton process mediated by Fe(III)-carboxylate complexes applied to degradation of landfill leachate, J. Environ. Chem. Eng. 5 (2017) 4462–4470, http://dx.doi.org/10.1016/j.jece.2017.08.043.

[11] W. Huang, M. Brigante, F. Wu, K. Hanna, G. Mailhot, Development of a new homogenous photo-Fenton process using Fe(III)-EDDS complexes, J. Photochem. Photobiol. A: Chem. 239 (2012) 17–23, http://dx.doi.org/10.1016/j.jphotochem.2012.04.018.

[12] J. Li, G. Mailhot, F. Wu, N. Deng, Photochemical efficiency of Fe(III)-EDDS complex : •OH radical production and 17β-estradiol degradation, J. Photochem. Photobiol. A: Chem. 212 (2010) 1–7, http://dx.doi.org/10.1016/j.jphotochem.2010.03.001.

[13] Y. Wu, M. Passananti, M. Brigante, W. Dong, G. Mailhot, Fe(III)–EDDS complex in Fenton and photo-Fenton processes: from the radical formation to the degradation of a target compound, Environ. Sci. Pollut. Res. 21 (2014) 12154–12162, http://dx.doi.org/10.1007/s11356-014-2945-1.

[14] N. Klamerth, S. Malato, A. Agüera, A. Fernández-Alba, Photo-Fenton and modified photo-Fenton at neutral pH for the treatment of emerging contaminants in wastewater treatment plant effluents: a comparison, Water Res. 47 (2013) 833–840, http://dx.doi.org/10.1016/j.watres.2012.11.008.

[15] S. Papoutsakis, S. Miralles-Cuevas, I. Oller, J.L. García Sánchez, C. Pulgarín, S. Malato, Microcontaminant degradation in municipal wastewater treatment plant secondary effluent by EDDS assisted photo-Fenton at near-neutral pH: An experimental design approach, Catal. Today. 252 (2015) 61–69, http://dx.doi.org/10.1016/j.cattod.2015.02.005.

[16] G. Rivas Ibáñez, M. Bittner, Z. Toušová, M.C. Campos-Mañas, A. Agüera, J.L. Casas,

J.A. Sánchez Pérez, K. Hilscherová, Does micropollutant removal by solar photo-Fenton reduce ecotoxicity in municipal wastewater? A comprehensive study at pilot scale open reactors, J. Chem. Technol. Biotechnol. 92 (2017) 2114–2122, http://dx.doi.org/10.1002/jctb.5212.

[17] I. De la Obra, L. Ponce-Robles, S. Miralles-Cuevas, I. Oller, S. Malato, J.A. Sánchez Pérez, Microcontaminant removal in secondary effluents by solar photo-Fenton at circumneutral pH in raceway pond reactors, Catal. Today 287 (2016) 10–14, http://dx.doi.org/10.1016/j.cattod.2016.12.028.

[18] P. Soriano-Molina, J.L. García Sánchez, S. Malato, L.A. Pérez-Estrada, J.A. Sánchez Pérez, Effect of volumetric rate of photon absorption on the kinetics of micropollutant removal by solar photo-Fenton with Fe^{3+}-EDDS at neutral pH, Chem. Eng. J. 331 (2018) 84–92, http://dx.doi.org/10.1016/j.cej.2017.08.096.

[19] O.M. Alfano, E.D. Albizzati, L.O. Conte, Modelling of Photo-Fenton Solar Reactors for Environmental Applications, in: D. Bahnemann, P. Robertson (Eds.), Environmental Photochemistry Part III. The Handbook of Environmental Chemistry, vol. 35, Springer, Berlin, Heidelberg, 2013, , http://dx.doi.org/10.1007/698_2013_246.

[20] F. Speck, S. Raja, V. Ramesh, V. Thivaharan, Modelling and Optimization of Homogenous Photo-Fenton Degradation of Rhodamine B by Response Surface Methodology and Artificial Neural Network, Int. J. Environ. Res. 10 (2016) 543–554, http://dx.doi.org/10.22059/ijer.2016.59683.

[21] S. Giannakis, I. Hendaoui, S. Rtimi, J.M. Fürbringer, C. Pulgarín, Modeling and treatment optimization of pharmaceutically active compounds by the photo-Fenton process: The case of the antidepressant Venlafaxine, J. Environ. Chem. Eng. 5 (2017) 818–828, http://dx.doi.org/10.1016/j.jece.2016.12.050.

[22] J.A. Sánchez Pérez, P. Soriano-Molina, G. Rivas, J.L. García Sánchez, J.L. Casas López, J.M. Fernández Sevilla, Effect of temperature and photon absorption on the kinetics of micropollutant removal by solar photo-Fenton in raceway pond reactors, Chem. Eng. J. 310 (2017) 464–472, http://dx.doi.org/10.1016/j.cej.2016.06.055.

[23] M. Simunovic, H. Kusic, N. Koprivanac, A.L. Bozic, Treatment of simulated industrial wastewater by photo-Fenton process: Part II. The development of mechanistic model, Chem. Eng. J. 173 (2011) 280–289, http://dx.doi.org/10.1016/j.cej.2010.09.030.

[24] L.O. Conte, A.V. Schenone, O.M. Alfano, Photo-Fenton degradation of the herbicide 2,4-D in aqueous medium at pH conditions close to neutrality, J. Environ. Manage. 170 (2016) 60–69, http://dx.doi.org/10.1016/j.jenvman.2016.01.002.

[25] L.O. Conte, A.V. Schenone, O.M. Alfano, Ferrioxalate-assisted solar photo-Fenton degradation of a herbicide at pH conditions close to neutrality, Environ. Sci. Pollut. Res. 24 (2017) 6205–6212, http://dx.doi.org/10.1007/s11356-016-6400-3.

[26] A.V. Schenone, L.O. Conte, M.A. Botta, O.M. Alfano, Modeling and optimization of photo-Fenton degradation of 2,4-D using ferrioxalate complex and response surface methodology (RSM), J. Environ. Manage. 155 (2015) 177–183, http://dx.doi.org/10.1016/j.jenvman.2015.03.028.

[27] S. Arzate, J.L. García Sánchez, P. Soriano-Molina, J.L. Casas López, M.C. Campos-Mañas, A. Agüera, J.A. Sánchez Pérez, Effect of residence time on micropollutant removal in WWTP secondary effluents by continuous solar photo-Fenton process in raceway pond reactors, Chem. Eng. J. 316 (2017) 1114–1121, http://dx.doi.org/10.1016/j.cej.2017.01.089.

[28] M.O. Barbosa, N.F.F. Moreira, A.R. Ribeiro, M.F.R. Pereira, A.M.T. Silva, Occurrence and removal of organic micropollutants: An overview of the watch list of EU Decision 2015/495, Water Res. 94 (2016) 257–279, http://dx.doi.org/10.1016/j.watres.2016.02.047.

[29] A.C.S.C. Teixeira, R. Guardani, C.A.O. Nascimento, Solar Photochemical Degradation of Aminosilicones Contained in Liquid EffluentsProcess Studies and Neural Network, Modeling, Ind. Eng. Chem. 42 (2003) 5751–5761, http://dx.doi.org/10.1021/ie0303350.

[30] A.J. Gutiérrez-Trashorras, E. Villicaña-Ortiz, E. Álvarez-Álvarez, J.M. González-Caballín, J. Xiberta-Bernat, M.J. Suarez-López, Attenuation processes of solar radiation. Application to the quantification of direct and diffuse solar irradiances on horizontal surfaces in Mexico by means of an overall atmospheric transmittance, Renew. Sustain. Energy Rev. 81 (2018) 93–106, http://dx.doi.org/10.1016/j.rser.2017.07.042.

[31] G. Rivas, I. Carra, J.L. García Sánchez, J.L. Casas López, S. Malato, J.A. Sánchez Pérez, Modelling of the operation of raceway pond reactors for micropollutant removal by solar photo-Fenton as a function of photon absorption, Appl. Catal. B: Environ. 178 (2015) 210–217, http://dx.doi.org/10.1016/j.apcatb.2014.09.015.

[32] M.I. Polo-López, I. García-Fernández, T. Velegraki, A. Katsoni, I. Oller, D. Mantzavinos, P. Fernández-Ibáñez, Mild solar photo-Fenton: An effective tool for the removal of *fusarium* from simulated municipal effluents, Appl. Catal. B: Environ. 111–112 (2012) 545–554, http://dx.doi.org/10.1016/j.apcatb.2011.11.006.

[33] S. Mitroka, S. Zimmeck, D. Troya, J.M. Tanko, How Solvent Modulates Hydroxyl Radical Reactivity in Hydrogen Atom Abstractions, J. Am. Chem. Soc. 132 (2010) 2907–2913, http://dx.doi.org/10.1021/ja903856t.

[34] O.M. Alfano, R.L. Romero, A.E. Cassano, A cylindrical photoreactor irrradiated from the bottom-I. Radiation flux density generated by a tubular source and a parabolic reflector, Chem. Eng. Sci. 40 (1985) 2119–2127, http://dx.doi.org/10.1016/0009-2509(85)87030-5.

[35] J. Colina-Márquez, F. Machuca-Martínez, G. Li Puma, Radiation absorption and optimization of solar photocatalytic reactors for environmental applications, Environ. Sci. Technol. 44 (2010) 5112–5120, http://dx.doi.org/10.1021/es100130h.

[36] I. Grčić, G. Li Puma, Photocatalytic Degradation of Water Contaminants in Multiple Photoreactors and Evaluation of Reaction Kinetic Constants Independent of Photon Absorption, Irradiance, Reactor Geometry, and Hydrodynamics, Environ. Sci. Technol. 47 (2013) 13702–13711, http://dx.doi.org/10.1021/es403472e.

[37] A. Cabrera Reina, L. Santos-Juanes, J.L. García Sánchez, J.L. Casas López, M.I. Maldonado Rubio, G. Li Puma, J.A. Sánchez Pérez, Modelling the photo-Fenton oxidation of the pharmaceutical paracetamol in water including the effect of photon absorption (VRPA), Appl. Catal. B: Environ. 166–167 (2015) 295–301, http://dx.doi.org/10.1016/j.apcatb.2014.11.023.

[38] A. Cabrera Reina, J.L. Casas López, M.I. Maldonado Rubio, L. Santos-Juanes Jordá, J.L. García Sánchez, J.A. Sanchez Pérez, Effects of environmental variables on the photo-Fenton plant design, Chem. Eng. J. 237 (2014) 469–477, http://dx.doi.org/10.1016/j.cej.2013.10.046.

[39] R.J. Brandi, M.A. Citroni, O.M. Alfano, A.E. Cassano, Absolute quantum yields in photocatalytic slurry reactors, Chem. Eng. Sci. 58 (2003) 979–985, http://dx.doi.org/10.1016/S0009-2509(02)00638-3.

[40] M.L. Satuf, R.J. Brandi, A.E. Cassano, O.M. Alfano, Photocatalytic degradation of 4-chlorophenol: A kinetic study, Appl. Catal. B: Environ. 82 (2008) 37–49, http://dx.doi.org/10.1016/j.apcatb.2008.01.003.

[41] C. Gueymard, SMARTS2, a Simple Model of the Atmospheric Radiative Transfer of Sunshine: Algorithms and Performance Assessment. Rep. FSEC-PF-270-95, Florida Solar Energy Center, Cocoa, USA, 1995.

[42] W. Huang, M. Brigante, F. Wu, C. Mousty, K. Hanna, G. Mailhot, Assessment of the Fe(III) − EDDS complex in Fenton-Like Processes: from the radical formation to the degradation of bisphenol A, Environ. Sci. Technol. 47 (2013) 1952–1959, http://dx.doi.org/10.1021/es304502y.

[43] D. Han, J. Wan, Y. Ma, Y. Wang, M. Huang, Enhanced decolorization of Orange g in a Fe(II)-EDDS activated persulfate process by accelerating the regeneration of ferrous iron with hydroxylamine, Chem. Eng. J. 256 (2014) 316–323, http://dx.doi.org/10.1016/j.cej.2014.06.006.

[44] Y. Zhang, N. Klamerth, S.A. Messele, P. Chelme-Ayala, M.G. El-Din, Kinetics study on the degradation of a model naphthenic acid by ethylenediamine- N, N'-disuccinic acid-modified Fenton process, J. Hazard. Mater. 318 (2016) 371–378, http://dx.doi.org/10.1016/j.jhazmat.2016.06.063.

[45] P. Cieśla, P. Kocot, P. Mytych, Z. Stasicka, Homogeneous photocatalysis by transition metal complexes in the environment, J. Mol. Catal. A: Chem. 224 (2004) 17–33, http://dx.doi.org/10.1016/j.molcata.2004.08.043.

[46] G.V. Buxton, C.L. Greenstock, W.P. Helman, A.B. Ross, Critical review of rate constants for reactions of hydrated electrons, hydrogen atoms and hydroxyl radicals ($^{\bullet}OH/^{\bullet}O^{-}$) in aqueous solution, J. Phys. Chem. Ref. Data 17 (1998) 513–886, http://dx.doi.org/10.1063/1.555805.

[47] R. Chen, J.J. Pignatello, Role of Quinone Intermediates as Electron Shuttles in Fenton and Photoassisted Fenton Oxidations of Aromatic Compounds, Environ. Sci. Technol. 31 (1997) 2399–2406, http://dx.doi.org/10.1021/es9610646.

[48] R.I.L. Eggen, J. Hollender, A. Joss, M. Schärer, C. Stamm, Reducing the discharge of micropollutants in the aquatic environment: the benefits of upgrading wastewater treatment plants, Environ. Sci. Technol. 48 (2014) 7683–7689, http://dx.doi.org/10.1021/es500907n.